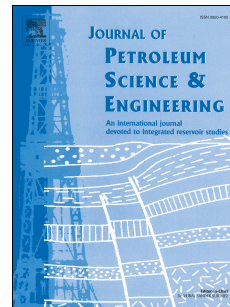


Accepted Manuscript

Capillary pressure and relative permeability estimation for low salinity waterflooding processes using pore network models

Edgar G. Martínez-Mendoza, Martín A. Díaz-Viera, Manuel Coronado, Ana T. Mendoza-Rosas



PII: S0920-4105(19)30665-5

DOI: <https://doi.org/10.1016/j.petrol.2019.106253>

Article Number: 106253

Reference: PETROL 106253

To appear in: *Journal of Petroleum Science and Engineering*

Received Date: 9 April 2019

Revised Date: 5 July 2019

Accepted Date: 7 July 2019

Please cite this article as: Martínez-Mendoza, E.G., Díaz-Viera, Martí.A., Coronado, M., Mendoza-Rosas, A.T., Capillary pressure and relative permeability estimation for low salinity waterflooding processes using pore network models, *Journal of Petroleum Science and Engineering* (2019), doi: <https://doi.org/10.1016/j.petrol.2019.106253>.

This is a PDF file of an unedited manuscript that has been accepted for publication. As a service to our customers we are providing this early version of the manuscript. The manuscript will undergo copyediting, typesetting, and review of the resulting proof before it is published in its final form. Please note that during the production process errors may be discovered which could affect the content, and all legal disclaimers that apply to the journal pertain.

Capillary pressure and relative permeability estimation for low salinity waterflooding processes using pore network models

Edgar G. Martínez-Mendoza^{a,*}, Martín A. Díaz-Viera^b, Manuel Coronado^b,
Ana T. Mendoza-Rosas^c

^aUniversidad Nacional Autónoma de México, Ciudad de México, México.

^bInstituto Mexicano del Petróleo, Eje Central Lázaro Cárdenas 152, 07730, Ciudad de México, México.

^cCONACYT-Centro de Ingeniería y Desarrollo Industrial, Av. Playa Pie de la Cuesta 702, 76125, Querétaro, México.

Abstract

In this work, the effect of low salinity water flooding (LSWF) on capillary pressure and relative permeability is studied at pore scale. For this purpose, a pore-scale model implemented on OpenPNM is developed to describe fluid flow, salinity transport and wettability change in a pore network. The effect is studied by considering high salinity waterflooding followed by low salinity waterflooding. The system wettability change is introduced as modifications of the local contact angle that are induced by the water salinity reduction. These modifications are evaluated by calculating the contact angle change in each pore and throat of the network, and then integrating it. From this analysis, a methodology has been developed to study the LSWF impact on capillary pressure and relative permeability. This methodology has been successfully applied to two pore network cases available in an open rock data base; one network correspond to a sandstone and the other to a carbonate sample. The methodology developed here can be seen as a tool to complement laboratory tests needed to determine the efficiency of LSWF processes.

*Corresponding author

Email addresses: edgarg.martinezm@gmail.com (Edgar G. Martínez-Mendoza), mdiazv@imp.mx (Martín A. Díaz-Viera), mcoronad@imp.mx (Manuel Coronado), ana.mendoza@cidesi.edu.mx (Ana T. Mendoza-Rosas)

Keywords: Low salinity waterflooding, pore network modeling, pore scale modeling, capillary pressure, relative permeability

1. Introduction

Low salinity waterflooding (LSWF) is an enhanced oil recovery (EOR) technique that mobilizes oil by reducing the salinity or modifying the composition of the injected water. The LSWF is considered as a simple and economical oil recovery technique due to the easy access to low salinity water sources, such as seawater (Al-Shalabi & Sepehrnoori, 2016; Nasralla et al., 2018). The LSWF potential was first recognized by Yildiz & Morrow (1996) and Tang & Morrow (1997), when they observed additional oil recovery in lab sandstone core floodings that has depended on injected water composition. Since then, LSWF has been successfully proven in laboratory flooding tests in sandstone and carbonate cores (Yildiz & Morrow, 1996; Tang & Morrow, 1997; Austad, 2013; Sheng, 2014; Sohal et al., 2016; Al-Shalabi & Sepehrnoori, 2016; Mahani et al., 2017), as well as in multiple sandstone reservoirs (Webb et al., 2004, 2005; Jerauld et al., 2008; Yousef et al., 2012; Aladasani et al., 2014). In many results, the oil recovery could be increased when injected water salinity was much lower than formation water salinity. Different mechanisms to explain the low salinity effect have been proposed (Austad, 2013; Sheng, 2014; Mahani et al., 2017). However, there is not yet a consensus on dominant LSWF mechanisms, and answers to many physics and chemistry questions are still pending (Sheng, 2014; Al-Shalabi & Sepehrnoori, 2016; Etemadi et al., 2017).

To date, several authors have simulated the LSWF process in lab cores (Jerauld et al., 2008; Wu & Bai, 2009; Mahani et al., 2011; Omekeh et al., 2012; Dang et al., 2013; Al-Shalabi & Sepehrnoori, 2016; Coronado & Díaz-Viera, 2017; Sanaei et al., 2018) using a mechanistic approach that parametrically modifies the relative permeability and capillary pressure curves as a function of salinity (Sheng, 2014). In all of these models, diverse macroscopic properties for the involved oil recovery mechanism were assumed. For example, they consider

spatially homogeneous rock-fluid properties, such as surface tension and contact angle, that importantly affect the capillary pressure and relative permeability curve behavior, which are key inputs in simulations. An alternative approach to evaluate the change on the capillary pressure and relative permeability due to LSWF is modeling the fluid flow and salinity transport at pore scale, which is the purpose of this work.

In general, pore-scale modeling is constituted by three main components: (i) description of the geometry and structure of the porous media, (ii) definition and solution of the governing equations, and (iii) selection of the macroscopic properties (Raoof, 2011). In this way, it is possible to incorporate porous medium properties that are underestimated at larger scales. Further, pore-scale modeling discretizes the porous structure by heterogeneously distributing voids with fluid phases inside, and its approaches are potentially attractive tools for dynamic property estimation, such as pore networks. Pore network modeling comprises various disciplines, such as spatial statistics, imaging and mathematical modeling, which contribute to characterize the desired phenomena, as is well described in examples given by M. Blunt and coworkers (Blunt et al., 2002; Okabe & Blunt, 2004; Valvatne et al., 2005; Gharbi & Blunt, 2012; Mostaghimi et al., 2012; Blunt et al., 2013; Raeini et al., 2017; Xie et al., 2017; Raeini et al., 2018). Part of Blunt's vast work focuses on imaging techniques and three-dimensional reconstructions applied in porous media. With these reconstructions and their coupling with mathematical models, Okabe & Blunt (2004); Valvatne et al. (2005); Mostaghimi et al. (2012) and Blunt et al. (2013) have studied Newtonian and non Newtonian flow in several rock samples (Okabe & Blunt, 2004; Valvatne et al., 2005; Mostaghimi et al., 2012; Blunt et al., 2013). In the same way, the pore network modeling application to other research areas includes: CO₂ sequestration (Kim & Santamarina, 2015), methane hydrate gas production (Mahabadi & Jang, 2014; Jang & Santamarina, 2014; Mahabadi et al., 2016a), gas bubble nucleation/migration (Zhao & Ioannidis, 2011), water retention curves (Dai & Santamarina, 2013; Kang et al., 2016; Mahabadi et al., 2016b), drying process in porous media (Yiotis et al., 2001), and polymer elec-

trolyte membranes for fuel cells (Gostick et al., 2006, 2007; Gostick & Weber, 60 2015).

In the last two decades, EOR modeling via pore networks has grown importantly and acquired great interest. In principle, this is due to two main factors: the computational developments and the improvement in the detailed description rock-fluid systems. With a proper physical-mathematical formulation, the 65 pore scale is able to capture some of the proposed EOR mechanisms that are not yet fully understood at larger scales, such as wettability alteration in rock-fluid systems. Bolandtaba & Skauge (2011) developed a network to study residual oil mobilization by polymer injection, where adsorption particle, entrapment by the polymer, and viscous forces were considered (Bolandtaba & Skauge, 2011). 70 Hammond & Unsal (2012) and Qin & Hassanizadeh (2015) studied different mechanisms for microbial enhanced oil recovery, where the surfactants in the rock-fluid system produced oil mobilization and wettability change (Hammond & Unsal, 2012; Qin & Hassanizadeh, 2015). Lu & Yortsos (2001) established a model to simulate in situ combustion of forward filtration, where the porous 75 microstructure and the solid fuel distribution effects on filtering combustion dynamics were investigated (Lu & Yortsos, 2001). Xu et al. (2018) modeled multiple physicochemical and thermal processes in combustion fronts in order to reduce potential risks in practical applications, such as high combustion temperature and low oxygen rate (Xu et al., 2018). Concerning the LSWF problem, 80 Sorbie & Collins (2010) proposed a detailed semiquantitative theory, based on theoretical considerations at pore scale, of how the LSWF effect works (Sorbie & Collins, 2010). Subsequently, Watson et al. (2011) addressed an uncertainty assessment on wettability alteration, which is one of the most discussed LSWF mechanisms. The generated network allows one to carry out a systematic investigation 85 of oil-water-rock parameters which are critical for oil recovery (Watson et al., 2011). Boujelben et al. (2018) described a dynamic model to investigate LSWF effects on oil recovery under dynamic flow conditions. Here, the salinity spatial distribution is tracked explicitly during the recovery process, and the fluid distribution is updated according to a relative balance between capillary

90 and viscous forces. Further, the capillary effects are correlated to salinity by relating contact angle and local injected water concentration ([Boujelben et al., 2018](#)).

In this paper a systematic methodology to simulate the LSWF process at pore scale is presented. This work is one of the first developments made to model 95 LSWF using pore networks. The methodology will provide a tool to observe the salinity effects on effective flow properties, and using it the LSWF effect on capillary pressure and relative permeability curves is studied. This paper is structured as follows. First, the pore network modeling details are presented. Second, the proposed methodology for LSWF is discussed. Finally, two cases 100 that show the methodology are presented. In these cases, fluid flow, salinity transport, and primary drainage are recreated to estimate absolute permeability, capillary pressure, and relative permeability curves.

2. Pore network modeling

Pore network modeling is an approach to study a wide range of phenomena, 105 taking into account both the medium's geometry and its connectivity. One of the main applications is to estimate effective flow and transport properties, such as capillary pressure curves, effective permeabilities, and effective diffusion coefficient, among others, which regularly are obtained by laboratory tests and experimental correlations.

110 The pore network modeling discretizes the porous medium morphology which is composed by its internal structure and its topology (the way in which the medium is connected) ([Sahimi, 2011](#)). In principle, the internal structure, which represents porosity, is constituted by pores and throats. The pores are defined as the larger voids connected by narrower paths called throats ([Blunt et al., 2013](#)). In general, the key parts of a pore network model are the pore structure 115 and the equations describing the phenomena, according to the study scale. The first part is commonly known as geometry, which expresses the medium connectivity and discretizes throats and pores by means of geometric entities

(Aker et al., 1998). The second part is the mathematical modeling that describes the phenomena in porous media. Coupling these elements adequately will allow optimal estimates (Arns et al., 2004; Martínez-Mendoza, 2016). In this paper, these two main elements are decomposed in order to gain a better overall model understanding. The elements involved are: (i) network, (ii) geometry, (iii) phases, (iv) pore-scale physics, and (v) methods (see Figure 1). The development of these five elements will enhance the overall pore network model. Briefly, each pore network element is described below.

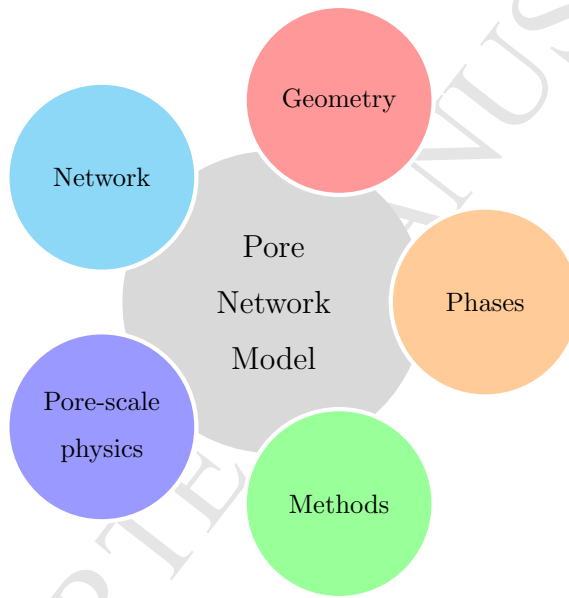


Figure 1: In general, the key elements of a pore network model are the medium structure and the mathematical models, and their adequate coupling can describe the phenomena at pore scale. In this work, these main elements are decomposed into: (i) network, (ii) geometry, (iii) phases, (iv) pore-scale physics, and (v) methods.

2.1. Network

It is the set of spatially localized void sites connected by bonds (Raoof et al., 2013). The network is the element that denotes the medium connectivity, it supports the model geometry and serves as simulation mesh. An important network property is the coordination number. The coordination number z de-

scribes the connectivity between sites and bonds, which means the number of bonds connected to a site.

2.2. Geometry

¹³⁵ Geometric entities placed in the network shape the internal medium structure. The network sites support the pores, while the bonds the throats. These elements can have both regular and irregular forms, being the former the one that offers a larger capability to describe the physical process. The irregular shapes can extend the study scope over processes that in a larger scale are ¹⁴⁰ negligible ([Sahimi, 2011](#)).

2.3. Phases

Depending on the process to be recreated, fluid or solid phases must be physically and chemically described by constitutive equations or correlations.

2.4. Pore-scale physics and methods

¹⁴⁵ To set the phase behavior at pore scale, the pore and throat geometry has to work together with proper definitions, physical laws, and constitutive equations; thus, suitable expressions for pore network models are obtained. All this is known as pore-scale physics ([Ioannidis & Chatzis, 1993](#); [Gostick et al., 2007](#)). By employing these assumptions, it becomes easier to establish methods that ¹⁵⁰ describe the nature of the desired events. Here, the phenomena of interest are fluid flow, salinity transport, and immiscible displacement.

3. Fluid flow and salinity transport modeling in pore networks

The LSWF process will be modeled as a decoupled flow and transport problem. From the fluid flow problem, pore pressure values will be computed, and ¹⁵⁵ they will be used in the transport problem to estimate the salinity concentration in both pores and throats. The concentration values will shape the salinity state in the network.

3.1. Conceptual model

The mathematical model considers a porous medium discretized by pores
 160 that are connected by narrower paths called throats, whose pore and throat
 geometry is invariant in time. Further, it is assumed that, during the whole
 process the porous medium is completely occupied by a fluid phase which con-
 tains only one dissolved component. The fluid flow and salinity transport will
 be solved in a decoupled way. The fluid flow through the network is under
 165 saturated conditions assuming laminar, Newtonian and single-phase flow. Af-
 ter imposing a pressure gradient between two opposite boundaries, a flow field
 in the network will take place. The salinity transport is inside the system is
 considered to follow advective-diffusive processes. Each network element (pores
 170 and throats) will be taken as a control volume, and salinity mass balance is
 solved over each element. Finally, a fully mixed domain is considered both in
 pores and in throats, therefore, a constant salinity gradient is assumed.

3.2. Mathematical formulation

3.2.1. Fluid flow

The fluid flow through pore network models assumes the Hagen-Poiseuille
 175 law, which describes laminar flow, q , of an incompressible and Newtonian fluid,
 under a pressure drop effect:

$$q = -\frac{\pi r^4 \Delta p}{8\mu l} \quad (1)$$

where r is the conduit radius, l is the conduit length, μ is the fluid viscosity,
 and p is the pressure. From this expression, the fluid hydraulic conductance κ
 follows as:

$$\kappa = \frac{\pi r^4}{8\mu l} \quad (2)$$

180 Considering a mass balance over each pore in the network, and using [Equation 1](#), yields:

$$\sum_{j=1}^n \kappa_{ij} (p_i - p_j) = 0 \quad (3)$$

where κ_{ij} is the total hydraulic conductance between pore i and pore j , whilst p_i and p_j are the pressures at each element. [Equation 3](#) denotes the fluid flow model for pore networks. The total hydraulic conductance is computed as the 185 hydraulic conductance sum through half of pore i , the connecting throat ij , and half of pore j . This parameter (κ_{ij}) depends on the size and the length of pores and throats.

[Equation 3](#) sets up the system of algebraic equations for the pressure value at each pore of the network to be solved. By this way the equation set $A\underline{x} = \underline{b}$ is obtained, where A is a banded matrix constituted by the hydraulic conductivities κ_{ij} , \underline{x} is the pore pressure vector, and \underline{b} contains the boundary condition values. After solving the system, the pore network model permeability is obtained by Darcy's law:

$$K = \frac{\mu Q L}{A(p_{in} - p_{out})} \quad (4)$$

where Q is the total flow across the network, A is the cross-sectional area normal to flow direction, L is the network length in the flow direction, p_{in} is the inlet pressure, and p_{out} is the outlet pressure. 195

3.2.2. Salinity transport

From the fluid flow problem, the pore pressure values are used to model the salinity advance via advective-diffusive transport.

200 For a given pore i , the one-component transport equation is:

$$V_i \frac{dc_i}{dt} + \sum_{j \in I_i}^{z_i} q_{ij} c_i - \sum_{j \in I_i}^{z_i} q_{ij} c_{ij} = \sum_{j \in I_i}^{z_i} D_e A_{ij} \frac{c_{ij} - c_i}{l_{ij}}, \quad \forall i \in [1, N_p] \quad (5)$$

where V_i and c_i are the volume and the salinity concentration for pore i , respectively. The flow rate and the salinity concentration throughout throat ij are denoted as q_{ij} and c_{ij} , respectively. D_e is the effective diffusion coefficient, A_{ij} is the connecting throat cross-sectional area, and l_{ij} is the connecting throat length. The total number of pores in the network is expressed as N_p , z_i is the pore coordination number, and I_i is the index set containing all the indexes of the pores connected to pore i through throat ij . 205

In the same way, the salinity transport equation for a given throat ij is:

$$V_{ij} \frac{dc_{ij}}{dt} + q_{ij}c_i + q_{ij}c_j - 2q_{ij}c_{ij} = D_e A_{ij} \frac{c_i - c_{ij}}{l_{ij}} + D_e A_{ij} \frac{c_j - c_{ij}}{l_{ij}}, \quad \forall i \in [1, N] \quad (6)$$

where V_{ij} is the volume and c_{ij} is the salinity concentration applying to throat ij , respectively, and c_j is the salinity concentration within pore j .

[Equation 5](#) and [Equation 6](#) comprise the mathematical model of fluid flow and salinity transport for pore networks, and their corresponding initial and boundary conditions are given by:

$$c(I, t_0) = c_0 \quad (7)$$

$$\begin{aligned} c(I_{inlet}, t \geq t_0) &= c_{inlet} \\ \left. \frac{dc}{dx} \right|_{I_{outlet}, t \geq t_0} &= 0 \end{aligned}$$

where I is the set of pore and throat indexes. I_{inlet} and I_{outlet} are the indexes of pores placed at the inlet and the outlet boundaries, respectively. The initial salinity concentration is denoted as c_0 , while the salinity concentration at the inlet is c_{inlet} . The initial time is expressed as t_0 .

3.3. Numerical discretization

A first order backward finite difference is applied in the numerical solution, therefore, a fully implicit solution scheme is obtained. For a given pore i , the discretized [Equation 5](#) can be written as:

$$V_i \frac{c_i^t - c_i^{t-1}}{\Delta t} = \sum_{j \in I_i}^{z_i} q_{ij} c_{ij}^t - \sum_{j \in I_i}^{z_i} q_{ij} c_i^t + \sum_{j \in I_i}^{z_i} D_e A_{ij} \frac{c_{ij}^t - c_i^t}{l_{ij}} \quad (8)$$

where the time step is denoted as Δt . Leaving only c_i^{t-1} on the left hand side of the [Equation 8](#), results:

$$c_i^{t-1} = c_i^t - \frac{\Delta t}{V_i} \left[\sum_{j \in I_i}^{z_i} q_{ij} c_{ij}^t - \sum_{j \in I_i}^{z_i} q_{ij} c_i^t + \sum_{j \in I_i}^{z_i} D_e A_{ij} \frac{c_{ij}^t - c_i^t}{l_{ij}} \right] \quad (9)$$

Similarly, the numerical discretization of [Equation 6](#) for a given throat ij is:

$$c_{ij}^{t-1} = c_{ij}^t - \frac{\Delta t}{V_{ij}} \left[q_{ij} c_i^t + q_{ij} c_j^t - 2q_{ij} c_{ij}^t + D_e A_{ij} \frac{c_i^t - c_{ij}^t}{l_{ij}} + D_e A_{ij} \frac{c_j^t - c_{ij}^t}{l_{ij}} \right] \quad (10)$$

²²⁵ The discretized initial and boundary conditions applied to [Equation 9](#) and [Equation 10](#) are:

$$c_i = c_0, \quad \forall i \in I_{pore}, \quad t = t_0 \quad (11)$$

$$c_{ij} = c_0, \quad \forall ij \in I_{throat}, \quad t = t_0$$

$$c_i = c_{inlet}, \quad \forall i \in I_{inlet}, \quad t \geq t_0$$

$$\sum_{j \in I_{outlet}}^{z_i} \frac{c_{ij}^t - c_i^t}{l_{ij}} = 0, \quad t \geq t_0$$

²³⁰ where I_{pore} and I_{throat} are the indexes of pores and throats, respectively. [Equation 9](#) and [Equation 10](#) lead to a linear system $A\underline{x} = \underline{b}$, where the number of unknown variables is equal to the total number of pores and throats $N_p + N_t$. Additionally, for scheme stability, the minimum time step is chosen on the basis of throat residence times ([Raoof, 2011; Acharya et al., 2005](#)):

$$\Delta t = \min \{ [V_{ij}] [q_{ij}^{-1}] \} = \min \{ T_{ij} \} \quad (12)$$

In [Equation 12](#), T_{ij} expresses the fluid residence time within throat ij . Since the advective-diffusive transport processes drive the salinity fluxes, the smallest throat, with higher flux rate, sets the time step ([Raoof et al., 2014](#)).

²³⁵ *3.4. Computational implementation*

The salinity transport model was implemented in OpenPNM which is an open-source pore network modeling package coded in Python. This package is fully independent of the network topology and dimensionality, since graph theory descriptors to represent the structure is used ([Gostick et al., 2016](#)). Furthermore, OpenPNM is designed to be customized; that is, users can code their own pore-scale physics and thermophysical property models ([Fazeli et al., 2016; Sadeghi et al., 2017; Tranter et al., 2016, 2018](#)). The validation of our implementation has been made against an 1D convective-dispersive solute transport equation provided by [van Genuchten & Alves \(1982\)](#) as described in [Appendix A](#).

4. Workflow to study a LSWF process

In this work the LSWF modeling involves evaluating the salinity impact on capillary pressure and relative permeability. By following a pore network based methodology, which is described in [Appendix B](#), a pore-scale physics to recreate a LSWF process is established ([Martínez-Mendoza, 2018](#)). The workflow to study LSWF processes is shown in [Figure 2](#) and listed as follows:

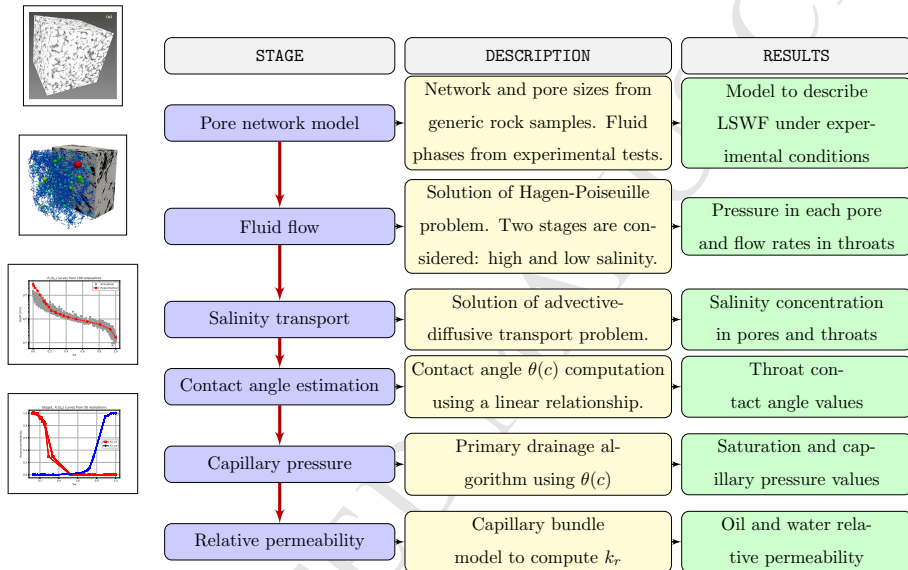


Figure 2: Workflow using the pore network approach to investigate low salinity waterflooding.

1. Pore network model: the network is mainly generated from imaging techniques. The open access data from two generic samples is used to set two case studies. The selection was based on the absolute permeability and the porosity values of the generic samples are close to information from experimental tests of our interest. The experiments study the injection of water with different salinity composition and its impact on oil recovery. Since these experiments were performed at lab scale, we only use their petrophysical information and description of the fluids to set our pore-scale models.

2. Fluid flow: to describe flow in the network, the model in [Equation 3](#) is used, and the simulation parameters and conditions were taken from the experimental tests. After solving this equation, the pressure in each pore and the flow rate in throats are obtained.
- 265 3. Salinity transport: by using the previous pressure values, the salinity transport equations ([Equation 5](#) and [Equation 6](#)) are solved. As a result, the salinity concentration, at different simulation times, at each pore and throat in the network is obtained. This information will allow the evaluation of the injection of water with different salinity composition. It should be noted that, since salinity transport effect on fluid flow is negligible, the pressure field should be computed only once, at the workflow start.
- 270 4. Contact angle evaluation: the wettability is evaluated by considering a linear relationship between contact angle (θ) and salinity concentration (c). This evaluation is an attempt to assess the salinity impact on contact angle.
- 275 5. Capillary pressure: a primary drainage process is simulated, at each time step of the salinity transport problem, in which an interest oil is the invading fluid and the injected water is the defending phase. After determining the invasion sequence, i.e. the water-invaded pores and throats, the capillary pressure curves for oil and water systems are estimated.
- 280 6. Relative permeability: the relative permeability curves are computed from the primary drainage invasion sequence and considering a capillary bundle model.

285 *4.1. Salinity effect on contact angle*

Wettability is the preferred tendency of a fluid to spread or adhere to a solid surface, in the presence of another immiscible fluid. A parameter that reflects such a preference is the contact angle θ . In pore-scale modeling, several mechanisms for wettability behavior have been proposed. In this work, the wettability change, and therefore the contact angle, is assumed as the principal

consequence of LSWF effects. In principle, the throat initial contact angle value could be changed when low salinity water invades the throat. As a result, reduction in capillary forces, that could affect oil recovery, would be expected if the contact angle change modifies the wettability to a less oil-wet system
²⁹⁵ (Boujelben et al., 2018). The following linear relationship between contact angle and salinity concentration is assumed (Aladasani et al., 2014):

$$\theta(c) = \theta^{HS} - \frac{c - c^{HS}}{c^{HS} - c^{LS}} (\theta^{HS} - \theta^{LS}) \quad (13)$$

where, θ^{HS} is the contact angle at the high salinity concentration, c^{HS} , and θ^{LS} is the contact angle at the low salinity concentration, c^{LS} .

4.2. Relative permeability

³⁰⁰ From the primary drainage capillary pressure and saturation data, we estimate the relative permeability curves using a bundle model. We consider the Rodríguez & Teyssier (1974) model which reproduces the displacement of a wetting fluid by a non wetting fluid in porous media (Rodríguez & Teyssier, 1974). The model can be written as:

$$j = \frac{\log \left(\int_{s_{wi}}^{s_w} \frac{ds_w}{p_c^2} / \int_{s_{wi}}^1 \frac{ds_w}{p_c^2} \right)}{\log \left(\frac{s_w - s_{wi}}{1 - s_{wi}} \right)} \quad (14)$$

$$k_{rw} = \left(\frac{s_w - s_{wi}}{1 - s_{wi}} \right)^{2+j} \quad (15)$$

$$k_{rnw} = \left[1 - \frac{s_w - s_{wi}}{1 - s_{wi}} \right]^2 \left[1 - \left(\frac{s_w - s_{wi}}{1 - s_{wi} - s_{nw}} \right)^j \right] \quad (16)$$

³¹⁰ where p_c is the capillary pressure, s_w is the wetting phase saturation, and s_{wi} is the irreducible wetting phase saturation. The subscript nw stands for the non wetting phase. Finally, k_{rw} and k_{rnw} refer to the wetting and the non wetting phase relative permeability, respectively.

5. Application to case studies

In this section the methodology is applied to two LSWF cases, one for sandstones and the other for carbonates. In the first case the capillary and relative

permeability curves are calculated and fitted for a sandstone-oil-water system.
 315 LSWF test information and fluid properties were taken from an experimental test, while the rock sample characteristics were taken from literature. In the carbonate second case, data from a LSWF lab test and open access information were used. The objective of these applications are: 1) demonstrate the model capacity to simulate a LSWF process at pore scale, and 2) observe the salinity
 320 effect on capillary pressure and relative permeability curves. The applications are described below.

5.1. Case 1: LSWF in a sandstone sample

This case seeks to introduce our methodology and shows a pore-scale LSWF study in sandstones. We used a laboratory-scale test in a sandstone core, where
 325 additional oil recovery is observed after a sequential injection of formation water and 100-times diluted formation water (Yousef et al., 2011). Further, open access information of a sandstone sample from a Middle East reservoir is used to generate the pore network model (Dong et al., 2007). However, not having the corresponding effective property measurements during the LSWF test (capillary pressure and relative permeability), our results establish an exploratory analysis on the expected values. The experimental test properties for Case 1
 330 are summarized in [Table 1](#).

In addition to the experimental test, we use the open access information of a generic sandstone sample from an Arabian reservoir (ICL, 2014b), which is
 335 here called Sample S1. Dong (2007) performed micro-computed tomography scanning of sandstone Sample S1 and several other rock samples (Dong, 2007). In this section, we use the extracted network and the pore and throat sizes from sandstone Sample S1, since its porosity and permeability values are close to those found in the sample of the experimental test. Details about the network
 340 model are presented in [Table 2](#).

A network of 1717 pores and 2824 throats discretizes the sandstone Sample S1, and it is used in the next computations. Pores are assumed to be spheres, while throats are represented as cylinders. Both entities share a circular cross-

Table 1: Information from an experimental test and Yousef et al. (2011) to set the case studies.

Property	Case 1	Case 2	Unit
Core length, L	0.049	0.041	m
Core diameter, d	0.038	0.038	m
Porosity, ϕ	0.18	0.25	m^3/m^3
Absolute permeability, k	6.46E-14	3.91E-14	m^2
Temperature, T	363.15	373.15	K
Pressure, p	17.2	12.4	MPa
Cross-sectional area, A	1.14E-03	1.14E-03	m^2
Volume, V	5.71E-05	4.63E-05	m^3
Pore volume, PV	1.05E-05	1.16E-05	m^3

section. The model porosity and permeability values are 14.35% and 1.53E-12 [m²], respectively. The pore network model is shown in Figure 3. Here, information from an experimental test was taken to establish the LSWF realization.

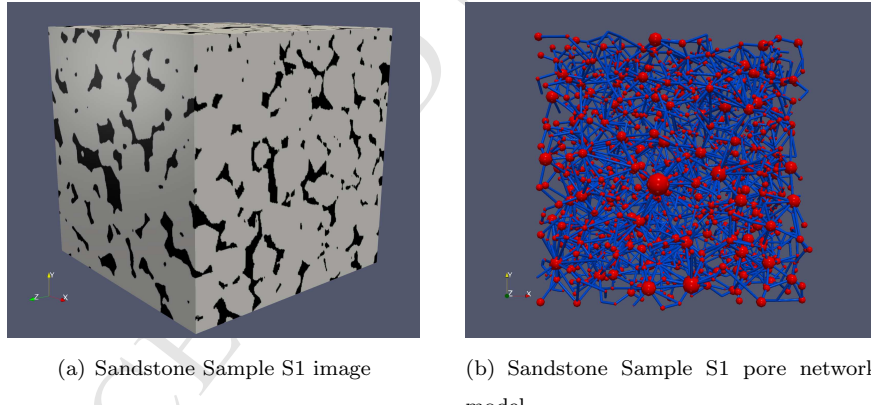


Figure 3: The generic sandstone Sample S1 used to simulate LSWF process in Case 1. (a) Micro CT image (ICL, 2014b). (b) Pore network model discretizing the sample, where spherical pores (red) and cylindrical throats (blue) are displayed.

The LSWF simulation considers two fluids that are injected sequentially into the network, which are formation water and formation water diluted 100 times. The formation water is the first fluid invading the network and has a high salinity

Table 2: Description of the pore network models used in case studies.

	Case 1 Sandstone Sample S1	Case 2 Carbonate Sample C2-Yousef
Network	Irregular	Irregular
	1717 pores	4311 pores
	2824 throats	7688 throats
	Volume = 1.76E-8 [m ³]	Volume = 9.77E-9 [m ³]
	Porosity = 14.35 (%)	Porosity = 24.41 (%)
	Absolute permeability = 1.53E-12 [m ²]	Absolute permeability = 3.76E-14 [m ²]
Geometry	Pores: spheres	
	Throats: cylinders	
	Cross section: circular	
	Pore/throat sizes from imaging	Pore/throat sizes from distributions
Physics	Capillary pressure: Young-Laplace	
	Hydraulic conductivity for cylinders	

350 concentration (HS). The low salinity fluid (LS) is the formation water diluted 100 times. The contact angle limit values for high and low salinity were taken from Moustafa et al. (2015). Moustafa et al. (2015) investigated the effect of several nanomaterials on contact angle for a sandstone sample (Moustafa et al., 2015). Table 3 summarizes the fluid properties used in Case 1.

Table 3: Fluid properties used in Case 1.

Property	Oil	Formation water	Formation water diluted 100 times	Unit	Reference
Density	881.6	1,130.0	1,013.8	kg/m ³	Experiment
Viscosity	1.08E-02	3.0E-04	4.85E-04	Pa.s	Experiment
Interfacial tension	—	0.0234	0.0172	N/m	Experiment
Contact angle	—	72	65	(°)	Moustafa et al. (2015)
Salinity concentration	—	216,000	2,160	ppm	Experiment

355 In the simulation, we solved the fluid flow and salinity transport problem in an uncoupled way; first the fluid flow is simulated in the network, and with the

Table 4: Parameters considered for LSWF process simulation in Case 1.

Parameter	HS	LS	Unit
Injection time (t_{inj})	7,000	7,000	s
Time step (Δt)	1	1	s
Initial salinity concentration (c_0)	0	c_{final}^{HS}	ppm
Salinity concentration at inlet (c_{in})	216,000	2,160	ppm
Neumann condition at outlet	0	0	ppm/m

resulting pressure field the salinity transport is then computed. The LSWF process begins invading the network with formation water, during a given injection time t_{inj} . Later, the diluted water is injected to start the recovery stage. Therefore, at the simulation ending, different concentration states for each time step are obtained; salinity concentration values are known in each pore and throat. Our simulation considers a four-hour LSWF process, 7000 [s] each stage; additional information regarding the simulation is shown in Table 4. In general, during the first stage the salinity concentration in the network increases until a steady-state at high salinity is reached. By starting the low salinity stage, the network concentration decreases, and most of the network elements reach the LS condition. Figure 4 displays the salinity in the network during the HS and LS stages, at two simulation times. The salinity concentration values are used to calculate the throat contact angle, where Equation 13 is used, it shows that as salinity decreases, contact angle also does. The contact angle change modifies the network wettability to a less oil-wet system. At the LSWF process end, the network has a homogeneous contact angle distribution. In addition, there are no abrupt θ changes in throats. In the HS stage a value equal to 72° is reached, while in LS stage the value is 65° . Considering the contact angle as an amount that denotes the wettability degree, we find that the sandstone's wettability, in HS and LS, is homogeneous. The latter can favor the residual oil displacement and, thereby, increase the oil recovery factor.

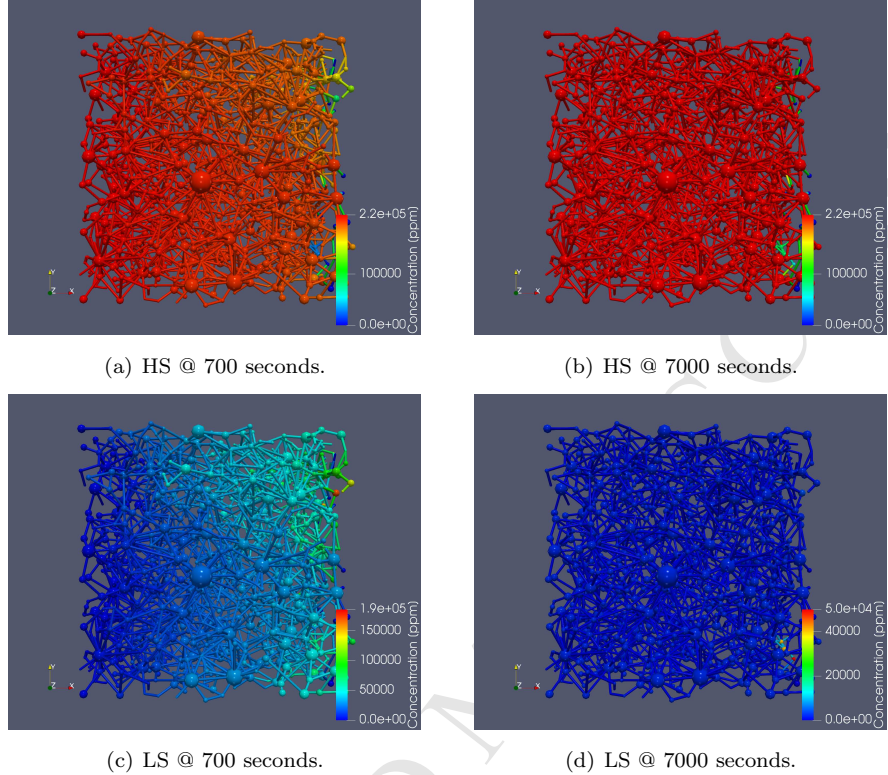
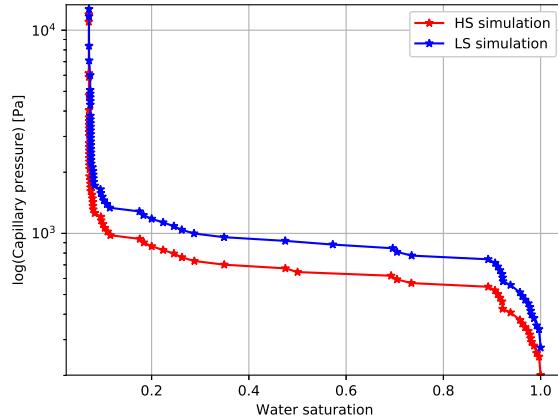


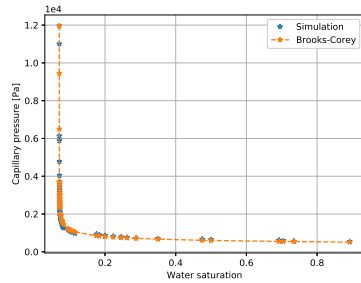
Figure 4: Salinity concentration in sandstone Sample S1 network during LSWF simulation for Case 1. HS stage simulation at (a) 700 and (c) 7000 seconds. LS stage simulation at (b) 700 and (d) 7000 seconds. The water flows from left to right.

According to the limiting contact angle values for the high and low salinity states (72° and 65° , respectively), the system is slightly intermediate wet when the HS fluid is the invading phase. After we switch to the LS fluid, a wettability change in the network is observed. At the LSWF process end, the system has gained stronger affinity to water. The corresponding capillary pressure curves are shown in Figure 5. The red curve in Figure 5(a) gives the LS initial condition, where the capillary pressure values range from 0.2 to 12 [kPa]. When the LS stage finishes (curve in blue), the irreducible water saturation is almost the same as the initial condition, with a value equal to 7%. However, higher pressure values are required to displace oil when the LSWF ends. It follows that the

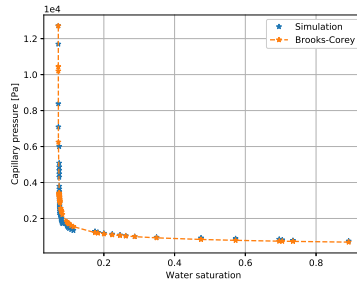
LSWF gives place to a slightly wettability modification in the network, because the LSWF produces an increase in preference towards water. Subsequently,
 390 we fitted a Brooks-Corey model to the initial and final LS curves. The fitted models can be used in simulations at larger scales. Table 5 summarizes the fitted Brooks-Corey parameters, and plots Figure 5(b) and Figure 5(c) show the fitted curves and the original data points.



(a) Capillary pressure



(b) Fitted HS capillary pressure curve



(c) Fitted LS capillary pressure curve

Figure 5: Capillary pressure curves for Case 1. (a) Capillary pressure curves showing the LSWF effect. The red curve is for the HS, while the blue curve for LS. In (b) and (c) the fitted Brooks-Corey $p_c(s_w)$ models for HS and LS, respectively. The blue points represent the values calculated in the primary drainage algorithm. The orange points are obtained using the fitted model. The dashed orange line shows the fitted curve trend.

Table 5: Fitting parameters for capillary pressure and relative permeability in HS and LS.

Parameter	Case 1		Case 2	
	HS	LS	HS	LS
Capillary pressure exponent	4.05	3.62	1.78	1.24
Entry pressure [Pa]	536	683	989	1,002
Water endpoint (k_{rw}^0)	0.35	0.65	0.15	0.40
Oil endpoint (k_{ro}^0)	0.97	0.96	0.98	0.99
Water exponent (n_w)	3.36	3.77	4.00	3.87
Oil exponent (n_o)	1.69	1.91	1.45	2.00
Residual water saturation (s_{wr})	0.07	0.07	0.26	0.27
Residual oil saturation (s_{or})	0.25	0.1	0.25	0.1

[Figure 6\(a\)](#) shows the estimated relative permeability curve, the solid lines are for HS and the dashed for LS. In the HS period, a residual oil saturation equal to 0.25 is obtained. The k_r curve crossing takes place when the water saturation s_w^{cross} is 0.53, in which $k_{ro}^{s_w^{cross}} = k_{rw}^{s_w^{cross}} = 0.11$. Further, the water and oil relative permeability endpoint is 0.32 and 0.97, respectively. For $s_w < 0.4$, k_{rw} values are almost zero, this points to a mixed wet system. In the LS stage, these properties undergo minimal changes. The s_{or} value decreases 60 percent, $s_{or} = 0.1$. The k_r curve crossing point occurs at a $s_w^{cross} = 0.57$, with $k_r = 0.11$. The curve endpoints are 0.96 and 0.65 for oil and water, respectively. This behavior is consistent with the wettability change in capillary pressure. Finally, from the stage end, we fitted a Brooks-Corey k_{rw} model and a modified Brooks-Corey k_{ro} model to the estimated curves. The fitted curves are shown in [Figure 6\(b\)](#) and [Figure 6\(c\)](#), and their respective parameters are summarized in [Table 5](#).

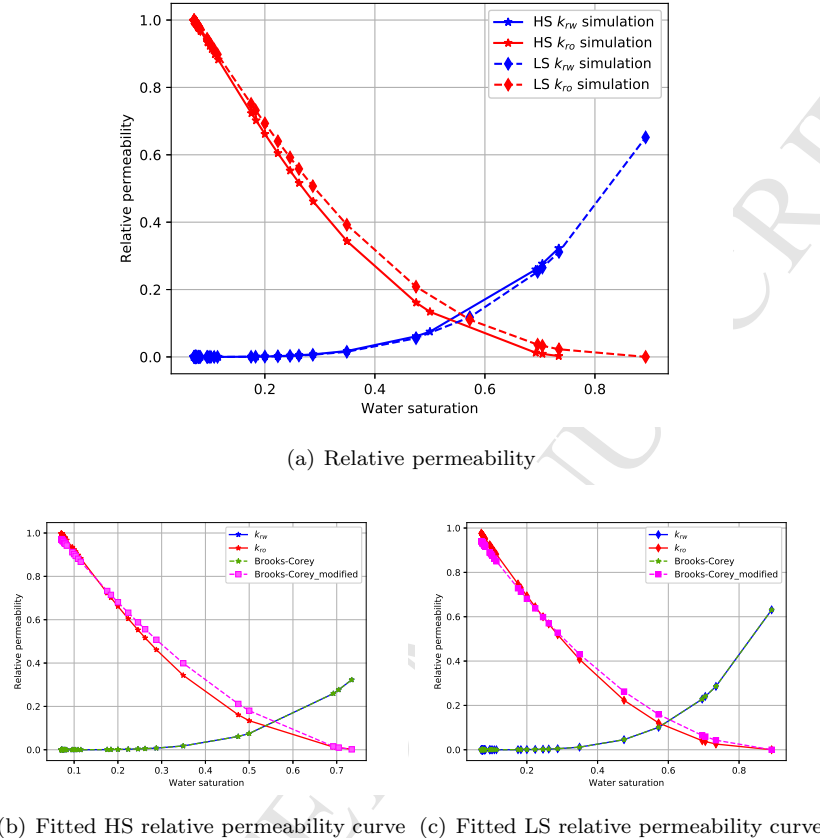
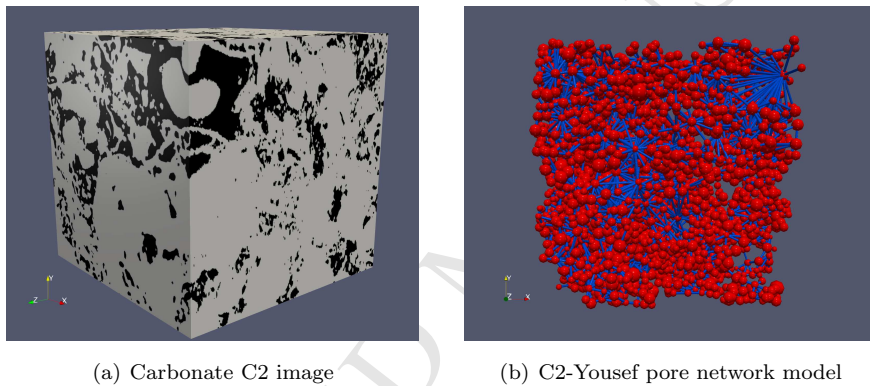


Figure 6: Relative permeability curves for Case 1. (a) The red lines show the oil relative permeability k_{ro} and the blue lines the water relative permeability k_{rw} . Solid lines correspond to HS and dashed lines to LS, and original data are in red and blue. The curves were fitted at the end of the (b) HS and (c) LS stages. In curve fitting, a Brooks-Corey k_{rw} model (green line) and a modified Brooks-Corey k_{ro} model (pink line) were used.

5.2. Case 2: LSWF in a carbonate sample

Through this case, we evaluate the LSWF impact on capillary pressure and relative permeability curves for a carbonate rock sample. Here we employ laboratory data from Yousef et al. (2011) and take the data for connate water and seawater for HS and LS, respectively, as well the data for viscosity, interfacial tension, contact angle, and salinity concentration. We use open access

information from a generic carbonate sample described as C2 (see [Figure 7\(a\)](#))
 415 ([ICL, 2014a](#)), and we fitted probability distribution functions for C2 pore and
 throat sizes. Subsequently, the fitted distribution parameters were modified, in
 order to reproduce the porosity and permeability values of [Yousef et al. \(2011\)](#).
 We straightforwardly use the C2 extracted network without any modification,
 keeping the network topology invariant, thus the proper carbonate topology is
 420 ensured. By using the extracted network in combination with the fitted proba-
 bility distribution, a new carbonate sample version is obtained, which is labeled
 as C2-Yousef in [Figure 7\(b\)](#).



[Figure 7](#): The synthetic carbonate Sample C2-Yousef used to simulate LSWF process in Case 2. (a) Micro CT image showing the carbonate C2 pore structure. (b) Pore network model C2-Yousef based on C2 structure. Spherical pores (red) and cylindrical throats (blue) are employed.

[Figure 8](#) shows the probability distribution functions for pore and throat size comparison between the carbonate C2 and the synthetic sample C2-Yousef.
 425 [Figure 8\(a\)](#) presents the pore diameter histograms, and [Figure 8\(b\)](#) shows the corresponding histograms for throat diameters. The carbonate C2 pore/throat diameters are those obtained and reported by [Dong \(2007\)](#). On the other hand, the diameter values for the C2-Yousef network were generated by probability distributions. The pore and throat size distribution of sample C2-Yousef was
 430 established by fitting a distribution to the original carbonate C2 data and then disturbing the fitting parameters. The distribution parameter selection was

made in a deterministic way until reaching absolute permeability and porosity values similar to Yousef et al. (2011) It is important to note that no spatial dependence is considered in this process. Table 6 summarizes the probability distribution parameters for samples C2 and C2-Yousef.

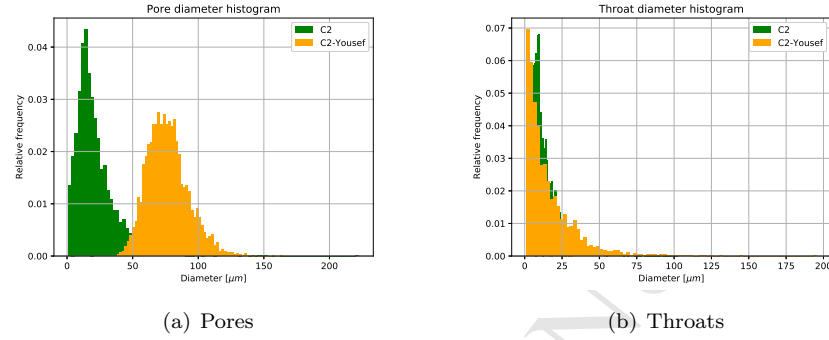


Figure 8: Pore and throat diameter histograms. (a) Comparison between C2 (green) and C2-Yousef (orange) pore diameters, and (b) the corresponding histograms for throat diameters.

Table 6: Probability distributions for pore and throat diameters in Case 2.

Property	Distribution	Shape	Location	Scale
C2 pores	Lognormal	0.6	-1.5	11
C2-Yousef pores	Lognormal	0.2	0	75
C2 throats	Lognormal	0.7	-0.3	5
C2-Yousef throats	Lognormal	0.9	1	30

The C2-Yousef network model consists of 8508 pores and 9818 throats, which are represented by spheres and cylinders, respectively. The model description is summarized in Table 2. In general, the network has highly dense areas of pores and throats, as well as considerable empty regions. This is attributed to the underlying complexity of carbonate pore structures. For this issue, image processing techniques have to treat microporosity and fractures in carbonates. In addition, if we wish to represent the porous structure by means of more complex pores and throats, it is necessary to take into account other geometric proper-

ties, such as angularity, inscribed and effective diameter, and shape factor. This
445 new information can only be obtained from high-resolution imaging techniques.

The simulation considers formation water with HS concentration (213,000 [ppm]), while seawater is the LS fluid, whose concentration is almost a quarter of that of HS (57,600 [ppm]). In addition, we use the same injection time and time step values from Case 1 ([Table 4](#)). The injected water information, for HS
450 and LS, was taken from [Yousef et al. \(2011\)](#), whose fluid property values are displayed in [Table 7](#).

Table 7: Fluid properties used in Case 2.

Property	Oil	Formation water	Seawater	Units	Reference
Density	873.0	1,108.3	1,015.2	kg/m ³	
Viscosity	1E-03	4.76E-4	2.72E-04	Pa.s	
Interfacial tension	—	0.0397	0.0339	N/m	Yousef et al. (2011)
Contact angle	—	92	80	(°)	
Salinity concentration	—	213,000	57,600	ppm	

[Figure 9](#) shows the salinity concentration in the network C2-Yousef during LSWF simulation. It is observed that, the water injection through the network is from left to right. According to the chosen time step, when the high salinity waterflooding (HSWF) ends, inlet pores and some neighboring pores reach the HS concentration (213,000 [ppm]), and a progressive concentration change in the network is observed. On the other hand, at the end of the LS process,
455 most of the network has a concentration close to 60,000 [ppm]. It is noteworthy the existence of pores and throats with concentration values being almost zero in both recovery processes (HS and LS). Intuitively, this is attributed to small enough throat sizes to constrain advective transport effects. In principle, for this particular case, these pores and throats constitute no-flow zones which do
460 not contribute for computing the absolute permeability.

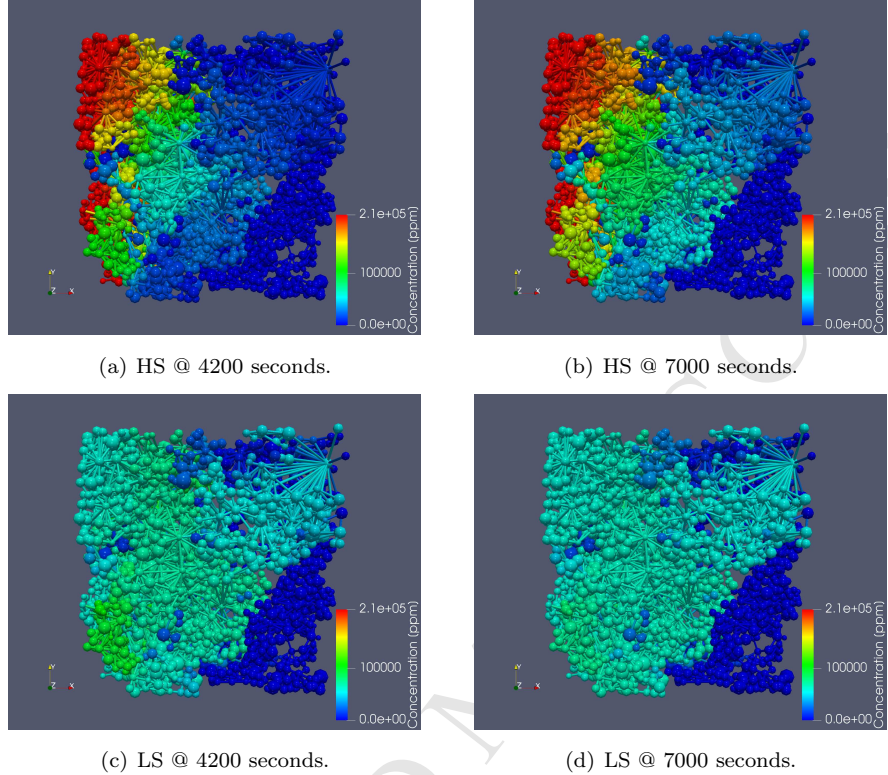


Figure 9: Salinity concentration in C2-Yousef network during LSWF simulation for Case 2. HS stage simulation at (a) 4200 and (c) 7000 seconds. LS stage simulation at (b) 4200 and (d) 7000 seconds. The water flows from left to right.

By running primary drainage algorithm uncoupled from the salinity transport, capillary pressure curves for each time step are estimated, and they are shown in [Figure 10](#). In this way, it is observe how the network salinity, which represents the LSWF process, displaces and modifies the capillary pressure curves. We link this event to a wettability change. At this scale, the wettability change impacts on modifying or reestablishing preferential flow zones, as well as an oil redistribution, since the capillary pressure in a given throat can be increased or decreased ([Boujelben et al., 2018](#)).

At the HS stage end, the C2-Yousef system remains with an intermediate wettability, but slightly preferring an oil contact; the maximum throat contact

angle value is $92^\circ > 90^\circ$. [Figure 10\(a\)](#) shows this effect, where the red curve is for the HSWF end, and in turn is the LSWF start. In this curve, capillary pressure values range from -5 to 25 [kPa]. This negative to positive value transition points out that oil prefers to be attached to the rock surface, when the system is totally saturated by water ($s_w \rightarrow 1$). As water saturation decreases, pressure increases and becomes positive. Therefore, the capillary pressure is positive and the wettability system changes from slightly oil wet to less oil wet, when $s_w < 0.8$. Subsequently, when the LS stage is completed, the capillary pressure curve is positive and shows an even less oil wettability (curve in blue). In general, at the LSWF end, the system has a slight preference towards water; that is, a minor wettability alteration occurs due to the LSWF process. However, it is difficult to establish a clear and significant wettability change for this case study, given that the contact angle value range ($92^\circ - 76^\circ$) is for intermediate wettability. [Figure 10\(b\)](#) and [Figure 10\(c\)](#) show the fitted $p_c(s_w)$ models for HS and LS, respectively, and [Table 5](#) summarizes the fitting parameters.

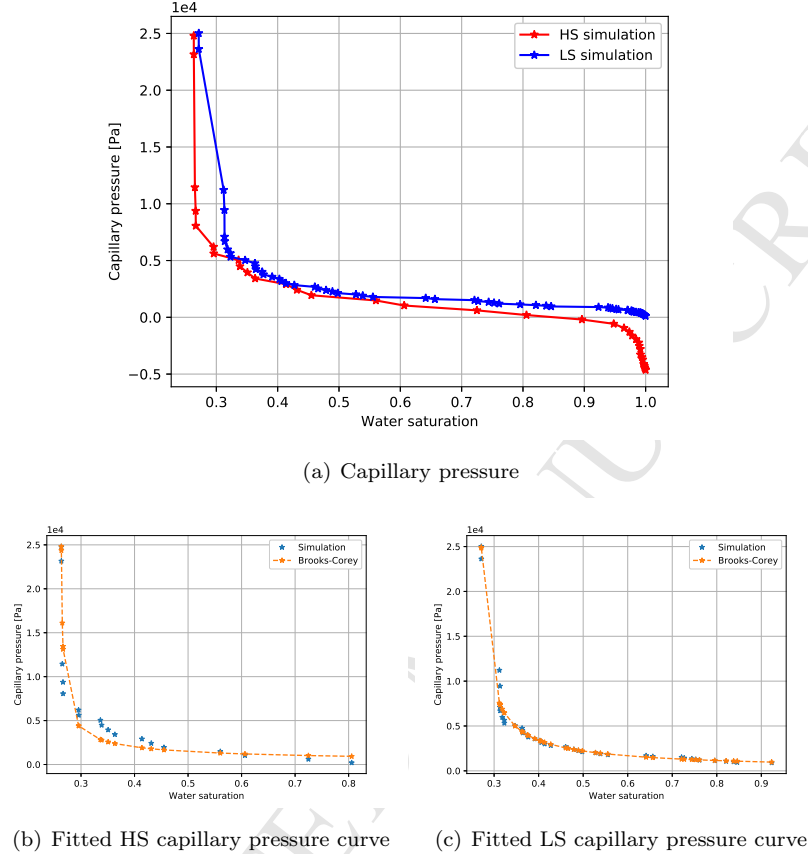


Figure 10: Capillary pressure curves for Case 2. (a) Capillary pressure curves showing the LSWF effect. The red curve is for HS, while the blue curve is for LS. Fitted Brooks-Corey $p_c(s_w)$ models for (b) HS (c) LS. The blue points represent the values calculated in the primary drainage algorithm. The orange points are obtained using the fitted model. The dashed orange line shows the fitted curve trend.

In Figure 11(a), at the LS stage start (solid line), the 72% water saturation points out that only the LS fluid can move through the network. In fact, the water relative permeability reaches 0.15, while the oil relative permeability is practically 0. Specifically, when $s_w = 72\%$, the oil saturation is 28%. This saturation value is known as critical oil saturation; that is, the saturation at which the oil begins to flow as the oil saturation increases. As water saturation

495 decreases, the water relative permeability also decreases, while the oil relative permeability increases. Another particular point on the relative permeability curve is $s_w = 26\%$, because at this saturation the water relative permeability becomes zero and the oil relative permeability is the maximum. This saturation is the critical water saturation and can be greater than or equal to the irreducible water saturation. At the LSWF end, the dashed line curves in [Figure 11\(a\)](#) show a slight shift to the right, compared to the initial curves (solid lines).
500 Regarding the initial state, the system has a subtle change in wettability, the curve crossing point moves from $s_w = 0.66$ to 0.68 . Moreover, prior the oil becomes mobile and comparing the initial state to the final, the water relative permeability endpoint moves from 0.15 to 0.40 . Finally, the k_r curves for HS and
505 LS are fitted ([Figure 11\(b\)](#) and [Figure 11\(c\)\(c\)](#), respectively), and the fitting parameters are summarized in [Table 5](#).

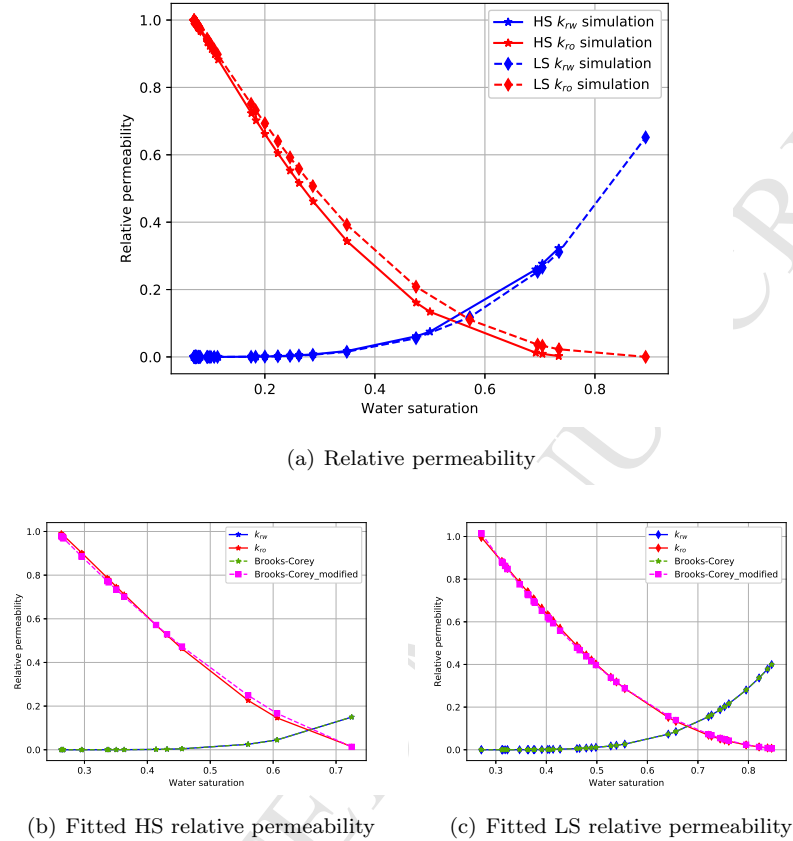


Figure 11: Relative permeability curves for Case 2. (a) The red lines show the oil relative permeability k_{ro} and the blue lines the water relative permeability k_{rw} . Solid lines correspond to HS and dashed lines to LS, and original data are in red and blue. The curves were fitted at the end of the (b) HS and (c) LS stages. In curve fitting, a Brooks-Corey k_{rw} model (green line) and a modified Brooks-Corey k_{ro} model (pink line) were used.

6. Conclusions

We have introduced a pore network based methodology to study the salinity effect on capillary pressure and relative permeability curves. Similarly, we formulated, implemented, and validated an advective-diffusive salinity transport model for pore networks. This model computes the salinity concentration values both in pores and throats. Since throats control the capillary pressure, knowing

the throat salinity concentration allows us to evaluate the salinity impact on the
 515 capillary pressure curves. The way we associate the salinity and the capillary pressure is through the contact angle, which is a linear function of the salinity concentration. The wettability of the network is modified by the changes in the contact angle, which in turn depends on the salinity. By reducing salinity the system becomes more water wet. By applying the methodology to two cases,
 520 one for a sandstone sample and the other for a carbonate sample, it has been demonstrated that our methodology can be used as a tool to rapidly estimate effective flow properties, which is an advantage over experimental procedures.

Nomenclature

Subscripts

525 0 Initial

e Effective

i, j ... Pore index

ij ... Throat index

iny .. Injection

530 p Pore

t Throat

Greek symbols

κ Hydraulic conductance

μ Viscosity

535 θ Contact angle

Symbols

A Cross-sectional area

D ... Diffusion coefficient

I Pore and throat indexes

540 K ... Absolute permeability

L Network length

l Throat length

p Pressure

Q ... Total flow

545 q Flow rate

r Radii

t Time

V ... Volume

Superscripts

550 HS .. High salinity

LS .. Low salinity

Appendix A. Validation

In this appendix the validation of the numerical code for the salinity convective-dispersive transport using a 1D network system is described. The analytical solution employed to validate [Equation 5](#) and [Equation 6](#) is that presented by [van Genuchten & Alves \(1982\)](#) for a pulse type injection. The equation is:

$$R \frac{\partial c}{\partial t} = D \frac{\partial^2 c}{\partial x^2} - V \frac{\partial c}{\partial x} \quad (\text{A.1})$$

[Equation A.1](#) is subjected to the initial and boundary conditions:

$$c(x, 0) = c_0 \quad (\text{A.2})$$

$$c(0, t) = \begin{cases} c_{iny} & 0 < t < t_{iny} \\ 0 & t > t_{iny} \end{cases}$$

$$\frac{\partial c(L, t)}{\partial x} = 0$$

where, t_{iny} and c_{iny} are the injection time and the salinity concentration during an injection period, respectively. The concentration at initial time is denoted as c_0 . The semi-analytical solution of [Equation A.1](#) is:

$$c(x, t) = \begin{cases} c_0 + (c_{iny} - c_0)A(x, t) & 0 < t < t_{iny} \\ c_0 + (c_{iny} - c_0)A(x, t) - c_{iny}A(x, t) & t > t_{iny} \end{cases} \quad (\text{A.3})$$

where

$$A(x, t) = 1 - \sum_{m=1}^{\infty} \frac{2\beta_m \sin\left(\frac{\beta_m x}{L}\right) \exp\left[\frac{vx}{2D} - \frac{v^2 t}{4DR} - \frac{\beta_m^2 D t}{L^2 R}\right]}{\left[\beta_m^2 + \left(\frac{vL}{2D}\right)^2 + \frac{vL}{2D}\right]} \quad (\text{A.4})$$

and where the eigenvalues β_m are the positive roots of the equation:

$$\beta_m \cot(\beta_m) + \frac{vL}{2D} = 0 \quad (\text{A.5})$$

In our validation, a 10-pore one-dimensional network and ideal conditions are established. The considered parameters are summarized in [Table A.8](#). Three 1000-iteration simulations were run for different time steps Δt , here 1, 0.1, and 0.01 [s] were employed. In this way, 1000, 100, and 10 [s] were considered as simulation times. To compare obtained results, concentration values at the outlet boundary were plotted for each time step ([Figure A.12](#)).

Table A.8: Parameters used in validation.

Property	Value	Unit
Initial concentration c_0	0	ppm
Injection concentration c_{inj}	200	ppm
Domain length L	1E-03	m
Injection time s	500, 50, and 5	s
Final time t_f	1000, 100, and 10	s
Time step Δt	1, 0.1, and 0.01	s
Injection velocity v	1.38E-04	m/s
Diffusion coefficient D	2.06E-08	m^2/s
R	1	

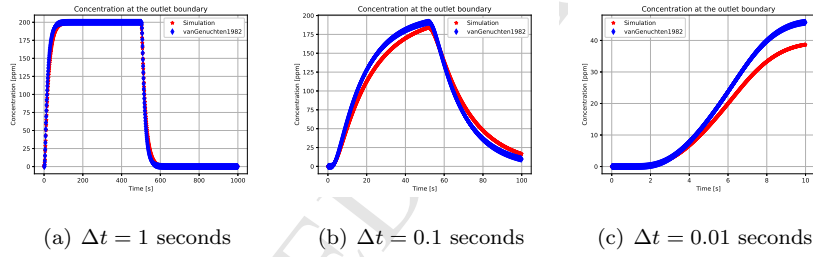


Figure A.12: Concentration at the outlet boundary for different time steps. (a) $\Delta t = 1$ [s], (b) $\Delta t = 0.1$ [s], and (c) $\Delta t = 0.01$ [s]. The plots show a comparison between the numerical simulation (red line) and the semi-analytical solution (blue line).

570 The comparison between the numerical simulation and the semi-analytical
 571 solution is shown in Figure 12(a), Figure 12(b) and Figure 12(c), where the so-
 572 lution using $\Delta t = 1, 0.1$, and 0.01 seconds, is respectively shown. By decreasing
 573 time step, Equation 5 and Equation 6 approach to the semi-analytical model.
 574 However, when $\Delta t = 0.01$ [s], the curves become separated at $t > 5$ [s]. But,
 575 since the mixtures are perfect and the reactions are neglected within pores and
 throats, this work does not require considering time steps below the thousandths
 of a second. Finally, according to computed errors summarized in Table A.9, it
 is agreed that the model (Equation 5 and Equation 6) is validated, providing

approximate values to the semi-analytical solution are obtained.

Table A.9: Computed error (%) from the numerical simulation and the semi-analytical solution.

Δt [s]	Absolute error	Relative error	Mean absolute error	Mean squared error
1	12	812	1	3
0.1	5	777	2	8
0.01	7	228	3	17

580 Appendix B. Modeling methodology using pore network models

In the literature, it has not been found a workflow that describes step by step the application of pore network models; however, common practices have been recognized. By following this review, fundamental procedures and techniques can be integrated and a methodology becomes apparent. It is noteworthy 585 that each methodology stage can be divided into more fields, thus allowing a better study range (Martínez-Mendoza, 2016). In Figure B.13, the solid red line points out the proposed methodology. However, depending on the ongoing stage, deviations from the proposed flow can be followed (dotted black lines). For example, a pore network can be generated directly from data acquisition 590 (extracted networks) without performing statistical analysis. Likewise, it is possible to create a network if the workflow starts from statistical analysis. Finally, after validation and uncertainty assessment, the workflow can turn back either data acquisition or statistical analysis in order to perform new realizations. The methodology stages are described below.

595 *Data acquisition*

In this stage, various properties that describe the porous medium, the fluids and the rock-fluid interactions are obtained. In pore network modeling, it becomes crucial to know the pore and the throat shapes and sizes, as well as the way in which these elements are connected. Therefore, the following pore 600 and throat properties must be defined: spatial location, coordination number,

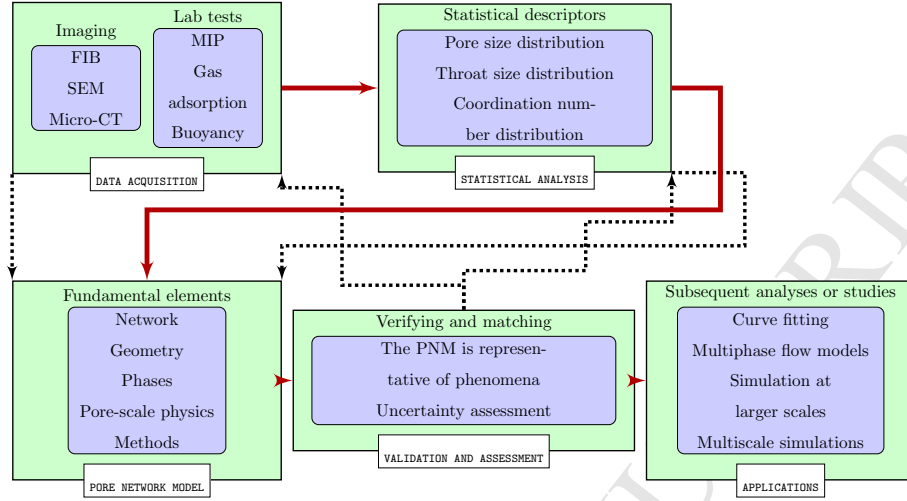


Figure B.13: Modeling methodology using pore networks. The methodology comprises five fundamental stages: data acquisition, statistical analysis of pore structure properties, pore network model, validation and uncertainty assessment, and applications.

area, inscribed diameter, perimeter, total length, volume, cross section, and shape factor. To characterize the porous medium there are high resolution imaging techniques such as scanning electron microscopy ($1 - 20 \text{ [nm]}$), focused ion beam ($< 1 \text{ [nm]}$), confocal laser scanning microscopy ($\sim 1 \text{ [\mu m]}$), X-ray computed micro-tomography ($1 - 200 \text{ [\mu m]}$), and nuclear magnetic resonance ($2 \text{ [nm]} - 1 \text{ [\mu m]}$) (Dong, 2007; Xiong et al., 2016). Applying these image techniques, the pore and the throat sizes, the network node coordinates and their connections with other nodes are inferred. Finally, to characterize the fluids and the rock-fluid system, laboratory tests to measure density, viscosity, interfacial tension, and contact angle, among other properties, are performed.

Statistical analysis of pore structure properties

This stage involves performing statistical analysis to main medium structure properties (e.g., throat and pore sizes, and coordination number) to fit probability distribution functions. The probability distribution functions generate the aforementioned property values, and consequently, a porous media analogous

to the original one can be achieved. In addition, performing network spatial statistical analysis to infer connectivity and percolation properties is highly recommended. With all this information it is possible different spatial realizations of the original sample.

⁶²⁰ *Pore network model*

From the previous stage an optimal framework for setting the fundamental pore network elements can be established. The complexity and detail with which the network and geometry are represented establish a starting point to formulate the pore-scale physics and consequently, the method scope. In principle, ⁶²⁵ the pore network models can be generated from three-dimensional reconstructions of rock samples and from their respective extracted network and geometry. Although this technique for pore network generation is established, it results in reality that the required information and tools are not fully available. Further, working with a unique extracted network could yield a narrow study window, ⁶³⁰ and the model cannot be representative. Hence, the statistical analysis represents an attractive option to generate different realizations for the network and the geometry. Finally, the simulations using these models can help to build a reliability window, which provides a value range that a desired property can take for a particular medium (e.g., absolute permeability, capillary pressure, ⁶³⁵ relative permeability).

Validation and uncertainty assessment

The validations of properties such as porosity, absolute permeability, capillary pressure, and relative permeability, can be achieved by comparing them against the corresponding laboratory test data. This comparison allows us to ⁶⁴⁰ verify that the implemented pore network model is representative of the phenomena. In addition, an uncertainty evaluation can be obtained by multiple simulations exploring the pore network parameters (e.g., the throat and pore size distributions).

Application in multiphase flow models

645 Finally, the obtained porosity, absolute permeability, capillary pressure, and relative permeability values can be used in subsequent analyzes, such as curve fitting, multiphase flow models, simulations at larger scales, and multiscale simulations.

References

- 650 Acharya, R., Van der Zee, S., & Leijnse, A. (2005). Transport modeling of non-linearly adsorbing solutes in physically heterogeneous pore networks. *Water Resour. Res.*, 41, 11. doi:[10.1029/2004WR003500](https://doi.org/10.1029/2004WR003500).
- Aker, E., Maloy, K., Hansen, A., & Batrouni, G. (1998). A two-dimensional network simulator for two-phase flow in porous media. *Transp. Porous Media*, 32, 163–186. doi:[10.1023/A:1006510106194](https://doi.org/10.1023/A:1006510106194).
- 655 Al-Shalabi, E. W., & Sepehrnoori, K. (2016). A comprehensive review of low salinity/engineered water injections and their applications in sandstone and carbonate rocks. *J. Pet. Sci. Eng.*, 139, 137–161. doi:[10.1016/j.petrol.2015.11.027](https://doi.org/10.1016/j.petrol.2015.11.027).
- 660 Aladasani, A., Bai, B., Wu, Y.-S., & Salehi, S. (2014). Studying low-salinity waterflooding recovery effects in sandstone reservoirs. *J. Pet. Sci. Eng.*, 120, 39–51. doi:[10.1016/j.petrol.2014.03.008](https://doi.org/10.1016/j.petrol.2014.03.008).
- Arns, J., Robins, V., Sheppard, A., Sok, R., Pinczewski, W., & Knackstedt, M. (2004). Effect of network topology on relative permeability. *Transp. Porous Media*, 55, 21–46. doi:[10.1023/B:TIPM.0000007252.68488.43](https://doi.org/10.1023/B:TIPM.0000007252.68488.43).
- 665 Austad, T. (2013). Water-Based EOR in Carbonates and Sandstones: New Chemical Understanding of the EOR Potential Using “Smart Water”. In J. J. Sheng (Ed.), *Enhanced Oil Recovery Field Case Studies* chapter 13. (pp. 301–335). Gulf Professional Publishing. doi:[10.1016/B978-0-12-386545-8.00013-0](https://doi.org/10.1016/B978-0-12-386545-8.00013-0).

- Blunt, M., Bijeljic, B., Dong, H., Gharbi, O., Iglauer, S., & Mostaghami, P. (2013). Pore-scale imaging and modeling. *Adv. Water Resour.*, *51*, 197–216. doi:[10.1016/j.advwatres.2012.03.003](https://doi.org/10.1016/j.advwatres.2012.03.003).
- Blunt, M., Jackson, M., Piri, M., & Valvatne, P. (2002). Detailed physics, predictive capabilities and macroscopic consequences for pore-network models of multiphase flow. *Adv. Water Resour.*, *25*, 1069–1089. doi:[10.1016/S0309-1708\(02\)00049-0](https://doi.org/10.1016/S0309-1708(02)00049-0).
- Bolandtaba, S. F., & Skauge, A. (2011). Network modeling of eor processes: A combined invasion percolation and dynamic model for mobilization of trapped oil. *Transp. Porous Media*, *89*, 357–382. doi:[10.1007/s11242-011-9775-0](https://doi.org/10.1007/s11242-011-9775-0).
- Boujelben, A., McDougall, S., Watson, M., Bondino, I., & Agenet, N. (2018). Pore network modelling of low salinity water injection under unsteady-state flow conditions. *J. Pet. Sci. Eng.*, *165*, 462–476. doi:[10.1016/j.petrol.2018.02.040](https://doi.org/10.1016/j.petrol.2018.02.040).
- Coronado, M., & Díaz-Viera, M. (2017). Modeling fines migration and permeability loss caused by low salinity in porous media. *J. Pet. Sci. Eng.*, *150*, 355–365. doi:[10.1016/j.petrol.2016.12.021](https://doi.org/10.1016/j.petrol.2016.12.021).
- Dai, S., & Santamarina, J. (2013). Water retention curve for hydrate-bearing sediments. *Geophys. Res. Lett.*, *40*, 5637–5641. doi:[10.1002/2013GL057884](https://doi.org/10.1002/2013GL057884).
- Dang, C., Nghiem, L., Chen, Z., & Nguyen, Q. (2013). Modeling low salinity waterflooding: Ion exchange, geochemistry and wettability alteration. *SPE*, *166447-MS*, 1–22. doi:[10.2118/166447-MS](https://doi.org/10.2118/166447-MS).
- Dong, H. (2007). Micro-ct imaging and pore network extraction. *Imperial College London*, (pp. 1–213). Unpublished thesis.
- Dong, H., Touati, M., & Blunt, M. (2007). Pore network modeling: Analysis of pore size distribution of arabian core samples. *SPE*, *105156-MS*, 1–5. doi:[10.2118/105156-MS](https://doi.org/10.2118/105156-MS).

- Etemadi, A., Khodapanah, E., & Tabatabaei-Nejad, S. A. (2017). Modelling low-salinity waterflooding: Effect of divalent cations and capillary pressure.
⁷⁰⁰ *J. Pet. Sci. Eng.*, *149*, 1–8. doi:[10.1016/j.petrol.2016.10.012](https://doi.org/10.1016/j.petrol.2016.10.012).
- Fazeli, M., Hinebaugh, J., & Bazylak, A. (2016). Incorporating embedded microporous layers into topologically equivalent pore network models for oxygen diffusivity calculations in polymer electrolyte membrane fuel cell gas diffusion layers. *Electrochim. Acta*, *216*, 364–375.
⁷⁰⁵ doi:[10.1016/j.electacta.2016.08.126](https://doi.org/10.1016/j.electacta.2016.08.126).
- van Genuchten, M., & Alves, W. (1982). Analytical solutions of the one-dimensional convective-dispersive solute transport equation. *United States Department of Agriculture, Economic Research Service, Technical Bulletin*, 1–152.
- ⁷¹⁰ Gharbi, O., & Blunt, M. J. (2012). The impact of wettability and connectivity on relative permeability in carbonates: A pore network modeling analysis. *Water Resour. Res.*, *48*, 1–14. doi:[10.1029/2012WR011877](https://doi.org/10.1029/2012WR011877).
- Gostick, J., Aghighi, M., Hinebaugh, J., Tranter, T., Hoeh, M. A., Day, H., Spellacy, B., Sharqawy, M. H., Bazylak, A., Burns, A., Lehnert, W., & Putz, A. (2016). Openpnm: A pore network modeling package. *Comput. Sci. Eng.*, *18*, 60–74. doi:[10.1109/MCSE.2016.49](https://doi.org/10.1109/MCSE.2016.49).
- Gostick, J., Ioannidis, M., Fowler, M., & Pritzker, M. (2007). Pore network modeling of fibrous gas diffusion layers for polymer electrolyte membrane fuel cells. *J. Power Sources*, *1*, 277–290. doi:[10.1016/j.jpowsour.2007.04.059](https://doi.org/10.1016/j.jpowsour.2007.04.059).
- ⁷²⁰ Gostick, J. T., Fowler, M. W., Ioannidis, M. A., Pritzker, M. D., Volkovich, Y., & Sakars, A. (2006). Capillary pressure and hydrophilic porosity in gas diffusion layers for polymer electrolyte fuel cells. *J. Power Sources*, *156*, 375 – 387. doi:[10.1016/j.jpowsour.2005.05.086](https://doi.org/10.1016/j.jpowsour.2005.05.086).
- Gostick, J. T., & Weber, A. Z. (2015). Resistor-network modeling of ionic

725 conduction in polymer electrolytes. *Electrochim. Acta*, *179*, 137–145.
doi:[10.1016/j.electacta.2015.03.126](https://doi.org/10.1016/j.electacta.2015.03.126).

Hammond, P., & Unsal, E. (2012). A dynamic pore network model for oil displacement by wettability-altering surfactant solution. *Transp. Porous Media*, *92*, 789–817. doi:[10.1007/s11242-011-9933-4](https://doi.org/10.1007/s11242-011-9933-4).

730 ICL (2014a). Imperial college consortium on pore-scale modelling: C2 carbonate. *PERM*, . URL: <http://www.imperial.ac.uk/earth-science/research/research-groups/perm/research/pore-scale-modelling/micro-ct-images-and-networks/carbonate-c2/>. doi:[10.6084/m9.figshare.1189258.v1](https://doi.org/10.6084/m9.figshare.1189258.v1).

735 ICL (2014b). Imperial college consortium on pore-scale modelling: S1 sandstone. *PERM*, . URL: <http://www.imperial.ac.uk/earth-science/research/research-groups/perm/research/pore-scale-modelling/micro-ct-images-and-networks/carbonate-c2/>. doi:[10.6084/m9.figshare.1189274.v1](https://doi.org/10.6084/m9.figshare.1189274.v1).

740 Ioannidis, M., & Chatzis, I. (1993). Network modelling of pore structure and transport properties of porous media. *Chem. Eng. Sci.*, *48*, 951–972. doi:[10.1016/0009-2509\(93\)80333-L](https://doi.org/10.1016/0009-2509(93)80333-L).

Jang, J., & Santamarina, J. (2014). Evolution of gas saturation and relative permeability during gas production from hydrate-bearing sediments: Gas invasion vs. gas nucleation. *J. Geophys. Res. Solid Earth*, *119*, 116–126. doi:[10.1002/2013JB010480](https://doi.org/10.1002/2013JB010480).

Jerauld, G., Webb, K., Lin, C., & Seccombe, J. (2008). Modeling low-salinity waterflooding. *SPE*, *11*, 1000–1012. doi:[10.2118/102239-PA](https://doi.org/10.2118/102239-PA).

745 Kang, D., Yun, T., Kim, K., & Jang, J. (2016). Effect of hydrate nucleation mechanisms and capillarity on permeability reduction in granular media. *Geophys. Res. Lett.*, *43*, 9018–9025. doi:[10.1002/2016GL070511](https://doi.org/10.1002/2016GL070511).

- Kim, S., & Santamarina, J. (2015). Reactive fluid flow in co2 storage reservoirs: A 2-d pore network model study. *Greenhouse Gas Sci. Technol.*, 5, 462–473. doi:[10.1002/ghg.1487](https://doi.org/10.1002/ghg.1487).
- 755 Lu, C., & Yortsos, Y. (2001). A pore-network model of in-situ combustion in porous media. *SPE, 69705-MS*, 1–16. doi:[10.2118/69705-MS](https://doi.org/10.2118/69705-MS).
- Mahabadi, N., Dai, S., Seol, Y., Sup Yun, T., & Jang, J. (2016a). The water retention curve and relative permeability for gas production from hydrate-bearing sediments: Pore-network model simulation. *Geochem. Geophys. Geosyst.*, 17, 3099–3110. doi:[10.1002/2016GC006372](https://doi.org/10.1002/2016GC006372).
- 760 Mahabadi, N., & Jang, J. (2014). Relative water and gas permeability for gas production from hydrate-bearing sediments. *Geochem. Geophys. Geosyst.*, 15, 2346–2353. doi:[10.1002/2014GC005331](https://doi.org/10.1002/2014GC005331).
- Mahabadi, N., Zheng, X., & Jang, J. (2016b). The effect of hydrate saturation 765 on water retention curves in hydrate-bearing sediments. *Geophys. Res. Lett.*, 43, 4279–4287. doi:[10.1002/2016GL068656](https://doi.org/10.1002/2016GL068656).
- Mahani, H., Keya, A. L., Berg, S., & Nasralla, R. (2017). Electrokinetics of 770 carbonate/brine interface in low-salinity waterflooding: Effect of brine salinity, composition, rock type, and ph on ζ -potential and a surface-complexation model. *SPE, 22*, 1–16. doi:[10.2118/181745-PA](https://doi.org/10.2118/181745-PA).
- Mahani, H., Sorop, T., Lighthelm, D., Brooks, D., Vledder, P., Mozahem, F., & Ali, Y. (2011). Analysis of field responses to low-salinity waterflooding in secondary and tertiary mode in syria. *SPE, 142960-MS*, 1–14. doi:[10.2118/142960-MS](https://doi.org/10.2118/142960-MS).
- 775 Martínez-Mendoza, E. G. (2016). Pore network models for obtaining effective flow and transport properties in petroleum reservoirs. *Universidad Nacional Autónoma de México, Faculty of Engineering(Bachelor)*, 103. Unpublished thesis.

- Martínez-Mendoza, E. G. (2018). Rock-fluid property estimation through pore
 780 network models for low salinity waterflooding process simulation. *Universidad
 Nacional Autónoma de México, Graduate Program in Earth Sciences(Master
 of Science)*, 146. Unpublished thesis.
- Mostaghimi, P., Bijeljic, B., & Blunt, M. (2012). Simulation of flow and dispersion
 on pore-space images. *SPE*, 17, 11. doi:[10.2118/135261-PA](https://doi.org/10.2118/135261-PA).
- Moustafa, E., Noah, A., Beshay, K., Sultan, L., Essam, M., & Nouh,
 785 O. (2015). Investigating the effect of various nanomaterials on the wettability
 of sandstone reservoir. *World J. Eng. Technol.*, 3, 116–126.
 doi:[10.4236/wjet.2015.33013](https://doi.org/10.4236/wjet.2015.33013).
- Nasralla, R. A., Mahani, H., van der Linde, H. A., Marcelis, F. H., Masalmeh,
 790 S. K., Sergienko, E., Brussee, N. J., Pieterse, S. G., & Basu, S. (2018).
 Low salinity waterflooding for a carbonate reservoir: Experimental evaluation
 and numerical interpretation. *J. Pet. Sci. Eng.*, 164, 640–654.
 doi:[10.1016/j.petrol.2018.01.028](https://doi.org/10.1016/j.petrol.2018.01.028).
- Okabe, H., & Blunt, M. J. (2004). Prediction of permeability for porous media
 795 reconstructed using multiple-point statistics. *Phys. Rev. E*, 70, 066135.
 doi:[10.1103/PhysRevE.70.066135](https://doi.org/10.1103/PhysRevE.70.066135).
- Omekeh, A., Friis, H., & Fjelde, S., I. adn Evje (2012). Modeling of ion-exchange
 and solubility in low salinity water flooding. *SPE*, 154144-MS,
 1–13. doi:[10.2118/154144-MS](https://doi.org/10.2118/154144-MS).
- Qin, C. Z., & Hassanzadeh, S. M. (2015). Pore-network modeling of solute
 800 transport and biofilm growth in porous media. *Transp. Porous Media*, 110,
 345–367. doi:[10.1007/s11242-015-0546-1](https://doi.org/10.1007/s11242-015-0546-1).
- Raeini, A. Q., Bijeljic, B., & Blunt, M. J. (2017). Generalized network modeling:
 Network extraction as a coarse-scale discretization of the void space of porous
 805 media. *Phys. Rev. E*, 96, 17. doi:[10.1103/PhysRevE.96.013312](https://doi.org/10.1103/PhysRevE.96.013312).

- Raeini, A. Q., Bijeljic, B., & Blunt, M. J. (2018). Generalized network modeling of capillary-dominated two-phase flow. *Phys. Rev. E*, *97*, 20. doi:[10.1103/PhysRevE.97.023308](https://doi.org/10.1103/PhysRevE.97.023308).
- Raoof, A. (2011). *Reactive/Adsorptive Transport in (Partially-) Saturated Porous Media; from pore scale to core scale*. Geologica Ultraiectina (1st ed.).
810 Utrecht University, Geosciences Faculty, Earth sciences department.
- Raoof, A., Nick, H., Hassanzadeh, S., & Spiers, C. (2013). Pore-flow: A complex pore-network model for simulation of reactive transport in variably saturated porous media. *Comp. Geosci.*, *61*, 160–174.
815 doi:[10.1016/j.cageo.2013.08.005](https://doi.org/10.1016/j.cageo.2013.08.005).
- Raoof, A., Nick, H. M., Hassanzadeh, S. M., & Spiers, C. J. (2014). Pore-network modeling of multi-component reactive transport under (variably-) saturated conditions. In R. Al-Khoury, & J. Bundschuh (Eds.), *Computational Models for CO₂ Geo-sequestration & Compressed Air Energy Storage*
820 Sustainable Energy Developments chapter 4. (pp. 137–170). London: CRC Press. (1st ed.).
- Rodríguez, F., & Teyssier, J. (1974). Permeabilidades relativas en función de la presión capilar y las saturaciones efectivas. *Ingeniería Petrolera*, *14*, 110–127.
- Sadeghi, M., Aghighi, M., Barralet, J., & Gostick, J. (2017). Pore network modeling of reaction-diffusion in hierarchical porous particles: The effects of microstructure.
825 *Chem. Eng. J.*, *330*, 1002–1011. doi:[10.1016/j.cej.2017.07.139](https://doi.org/10.1016/j.cej.2017.07.139).
- Sahimi, M. (2011). *Flow and Transport in Porous Media and Fractured Rock*. (2nd ed.). Wiley-VCH.
- Sanaei, A., Tavassoli, S., & Sepehrnoori, K. (2018). Investigation of modified water chemistry for improved oil recovery: Application of dlvo theory and surface complexation model. *SPE*, (pp. 1–27). doi:[10.2118/190017-MS](https://doi.org/10.2118/190017-MS).
830

- Sheng, J. (2014). Critical review of low-salinity waterflooding. *J. Pet. Sci. Eng.*, *120*, 216–224. doi:[10.1016/j.petrol.2014.05.026](https://doi.org/10.1016/j.petrol.2014.05.026).
- 835 Sohal, M. A., Thyne, G., & Sogaard, E. G. (2016). Review of recovery mechanisms of ionically modified waterflood in carbonate reservoirs. *Energy Fuels*, *30*, 1904–1914. doi:[10.1021/acs.energyfuels.5b02749](https://doi.org/10.1021/acs.energyfuels.5b02749).
- Sorbie, K., & Collins, I. (2010). A proposed pore-scale mechanism for how low salinity waterflooding works. *SPE*, *129833-MS*, 1–18. doi:[10.2118/129833-MS](https://doi.org/10.2118/129833-MS).
- 840 Tang, G., & Morrow, N. (1997). Salinity, temperature, oil composition, and oil recovery by waterflooding. *SPE*, *12*, 1–8. doi:[10.2118/36680-PA](https://doi.org/10.2118/36680-PA).
- Tranter, T., Gostick, J., Burns, A., & Gale, W. (2016). Pore network modeling of compressed fuel cell components with openpnm. *Fuel Cells*, *16*, 504–515. doi:[10.1002/fuce.201500168](https://doi.org/10.1002/fuce.201500168).
- 845 Tranter, T., Gostick, J., Burns, A., & Gale, W. (2018). Capillary hysteresis in neutrally wettable fibrous media: A pore network study of a fuel cell electrode. *Transp. Porous Media*, *121*, 597–620. doi:[10.1007/s11242-017-0973-2](https://doi.org/10.1007/s11242-017-0973-2).
- Valvatne, P., Piri, M., Lopez, X., & Blunt, M. (2005). Predictive pore-scale modeling of single and multiphase flow. *Transp. Porous Media*, *58*, 23–41. doi:[10.1007/s11242-004-5468-2](https://doi.org/10.1007/s11242-004-5468-2).
- Watson, M., Bondino, I., Hamon, G., & McDougall, S. (2011). A pore-scale investigation of low-salinity waterflooding in porous media: Uniformly wetted systems. *Transp. Porous Media*, *118*, 201–223. doi:[10.1007/s11242-017-0854-8](https://doi.org/10.1007/s11242-017-0854-8).
- 850 Webb, K., Black, C., & Edmonds, I. (2005). Low salinity oilrecovery: The role of reservoir condition corefloods. *EAGE Symposium on Improved Oil Recovery*, *Paper C18*.

- Webb, K. J., Black, C. J. J., & Al-Ajeel, H. (2004). Low salinity oil recovery -
 860 log-inject-log. *SPE, 89379-MS*, 1–7. doi:[10.2118/89379-MS](https://doi.org/10.2118/89379-MS).
- Wu, Y., & Bai, B. (2009). Efficient simulation for low salinity water-flooding in porous and fractured reservoirs. *SPE, 118830-MS*, 1–13.
 doi:[10.2118/118830-MS](https://doi.org/10.2118/118830-MS).
- Xie, C., Raeini, A. Q., Wang, Y., Blunt, M. J., & Wang, M. (2017). An improved pore-network model including viscous coupling effects using direct simulation by the lattice boltzmann method. *Adv. Water Resour.*, *100*, 26–34. doi:[10.1016/j.advwatres.2016.11.017](https://doi.org/10.1016/j.advwatres.2016.11.017).
- Xiong, Q., Baychev, T. G., & Jivkov, A. P. (2016). Review of pore network modelling of porous media: Experimental characterisations, network constructions
 865 and applications to reactive transport. *J. Contam. Hydrol.*, *192*, 101–117.
 doi:[10.1016/j.jconhyd.2016.07.002](https://doi.org/10.1016/j.jconhyd.2016.07.002).
- Xu, Q., Long, W., Jiang, H., Zan, C., Huang, J., Chen, X., & Shi, L. (2018). Pore-scale modelling of the coupled thermal and reactive flow at the combustion front during crude oil in-situ combustion. *Chem. Eng. J.*, *350*, 776–790.
 875 doi:[10.1016/j.cej.2018.04.114](https://doi.org/10.1016/j.cej.2018.04.114).
- Yildiz, H. O., & Morrow, N. R. (1996). Effect of brine composition on recovery of moutray crude oil by waterflooding. *J. Pet. Sci. Eng.*, *14*, 159–168.
 doi:[10.1016/0920-4105\(95\)00041-0](https://doi.org/10.1016/0920-4105(95)00041-0).
- Yiotis, A., Stubos, A., Boudouvis, A., & Yortsos, Y. (2001). A 2-d pore-network
 880 model of the drying of single-component liquids in porous media. *Adv. Water Resour.*, *24*, 439–460. doi:[10.1016/S0309-1708\(00\)00066-X](https://doi.org/10.1016/S0309-1708(00)00066-X).
- Yousef, A. A., Al-Saleh, S. H., Al-Kaabi, A., & Al-Jawfi, M. S. (2011). Laboratory investigation of the impact of injection-water salinity and ionic content on oil recovery from carbonate reservoirs. *SPE*, *14*, 1–16.
 885 doi:[10.2118/137634-PA](https://doi.org/10.2118/137634-PA).

- Yousef, A. A., Liu, J. S., Blanchard, G. W., Al-Saleh, S., Al-Zahrani, T., Al-Zahrani, R. M., Al-Tammar, H. I., & Al-Mulhim, N. (2012). Smart Water-flooding: Industry. *SPE, 159526-MS*, 1–26. doi:[10.2118/159526-MS](https://doi.org/10.2118/159526-MS).
- Zhao, W., & Ioannidis, M. A. (2011). Gas exsolution and flow during super-saturated water injection in porous media: I. pore network modeling. *Adv. Water Resour.*, *34*, 2–14. doi:[10.1016/j.advwatres.2010.09.010](https://doi.org/10.1016/j.advwatres.2010.09.010).

Highlights

- The effect of low salinity water flooding (LSWF) on capillary pressure and relative permeability is studied.
- An advective-diffusive salinity transport model for pore networks is developed.
- A pore network based methodology to describe LSWF processes is established.
- This methodology can be used as a tool to rapidly estimate effective flow properties.